Nuclear quantum effects in structural and elastic properties of cubic silicon carbide

Carlos P. Herrero ⬤,[1,*] Rafael Ramírez ⬤,[1] and Gabriela Herrero-Saboya[2]

[1]*Instituto de Ciencia de Materiales de Madrid, Consejo Superior de Investigaciones Científicas (CSIC),*
Campus de Cantoblanco, 28049 Madrid, Spain

[2]*CNR-IOM Democritos National Simulation Center, Istituto Officina dei Materiali, c/o SISSA, via Bonomea 265, IT-34136 Trieste, Italy*

Silicon carbide, a semiconducting material, has gained importance in the fields of ceramics, electronics, and renewable energy due to its remarkable hardness and resistance. In this study, we delve into the impact of nuclear quantum motion, or vibrational mode quantization, on the structural and elastic properties of $3C$-SiC. This aspect, elusive in conventional *ab initio* calculations, is explored through path-integral molecular dynamics (PIMD) simulations using an efficient tight-binding (TB) Hamiltonian. This investigation spans a wide range of temperatures and pressures, including tensile stress, adeptly addressing the quantization and anharmonicity inherent in solid-state vibrational modes. The accuracy of the TB model has been checked by comparison with density-functional-theory calculations at zero temperature. The magnitude of quantum effects is assessed by comparing PIMD outcomes with results obtained from classical molecular dynamics simulations. Our investigation uncovers notable reductions of 5%, 10%, and 4% in the elastic constants C_{11}, C_{12}, and C_{44}, respectively, attributed to atomic zero-point oscillations. Consequently, the bulk modulus and Poisson's ratio of $3C$-SiC exhibit reduced values by 7% and 5% at low temperatures. The persistence of these quantum effects in the material's structural and elastic attributes beyond room temperature underscores the necessity of incorporating nuclear quantum motion for an accurate description of these fundamental properties of SiC.

I. INTRODUCTION

Bulk silicon carbide is recognized as a semiconducting material with outstanding physical properties, such as low thermal expansion, high strength, thermal conductivity, and refractive index [1]. It exists in more than 250 different polytypes, many of which have hexagonal or rhombohedral crystalline structures. Moreover, there has been an increasing interest in other materials consisting of carbon and silicon, such as nanotubes, fullerenes, and two-dimensional structures [1–5].

Mechanical properties of bulk SiC have been intensively studied over the years using experimental techniques [6–9] and theoretical approaches [10–16], due to their significance in both basic research and various technological applications, including heat shielding, nuclear fuel particles, filament pyrometry, telescope mirrors, electric systems, and electronic devices. In general, the behavior of semiconducting solids under high pressure conditions has recently received renewed attention as potential constituents of carbon-rich exoplanets, as extreme planetary interior conditions can significantly influence their physical properties [17,18].

One of the most prevalent forms of silicon carbide, stable under ambient conditions, is cubic $3C$-SiC. Extensive research has been conducted on this polytype, employing various computational techniques, with a notable focus on density-functional theory (DFT) calculations at $T = 0$ [11,14,19,20]. Since accounting for finite temperatures requires the estimation of vibrational modes within a quasi-harmonic

approximation [12,21–23], these methods are reliable at low temperatures where anharmonic effects are relatively small, but their accuracy can diminish due to increasing anharmonicity as the temperature rises.

Numerous studies investigating the finite-temperature characteristics of SiC have relied on classical atomistic simulations [13,24–28]. However, it is noteworthy that the Debye temperature Θ_D of silicon carbide greatly exceeds room temperature ($\Theta_D \approx 1100$ K for cubic SiC [29]). As a result, the interplay of nuclear quantum effects (or phonon quantization) and anharmonicities in the interatomic potential is expected to impact the material's physical properties at temperatures relatively high, potentially on the order of, or even surpassing, room temperature. The constraints posed by classical atomistic simulations can be surmounted by methods explicitly accounting for nuclear quantum motion. Such is the case for computational techniques grounded in Feynman path integrals [30–33]. These techniques have gained prominence in recent years for exploring diverse material properties, including silicon [34], boron nitride [35,36], diamond [37,38], and graphene [32,33,39].

In this paper, we employ the path-integral molecular dynamics (PIMD) technique to investigate the structural and elastic properties of $3C$-SiC across temperatures ranging from $T = 50$ to 1500 K, and hydrostatic pressures spanning from $P = -30$ GPa (tension) to 60 GPa (compression). The interatomic interactions in our simulations are described by an effective tight-binding (TB) Hamiltonian. To assess the precision of the TB outcomes, we have also carried out DFT calculations at $T = 0$. Nuclear quantum effects are assessed by contrasting the findings from PIMD simulations with those

---

*ch@icmm.csic.es

derived from classical molecular dynamics (MD) simulations using the same TB Hamiltonian. Furthermore, we scrutinize the impact of anharmonicity on the physical properties of cubic SiC by comparing our results against those attained through a harmonic approximation. Our findings reveal that quantum corrections induce a significant reduction in the elastic constants, bulk modulus, and Poisson's ratio at low temperatures. These quantum effects demonstrate their notable presence in the structural and elastic properties of 3C-SiC, remaining appreciable at temperatures surpassing 300 K.

Similar path-integral simulations, akin to those presented in this paper, have been previously employed to examine nuclear quantum effects in carbon-based materials [32,33,37,38,40], silicon [34], and boron nitride [36,41]. These effects exhibit significance in electronic gaps [42] and in the isotope dependence of the lattice parameter in cubic SiC [43]. Here, we advance the understanding of nuclear quantum effects in various properties of materials with cubic symmetry, such as 3C-SiC. In particular, we expand the region of studied pressures to include tensile stress, allowing us to investigate this material in a metastable region of the P-T phase diagram. This exploration yields information on the attractive region of the interatomic potential. In contrast to earlier simulations of this kind, we present a detailed comparison of TB results with those obtained from DFT calculations at $T = 0$, providing a more solid foundation for the data derived from PIMD simulations. Moreover, the consideration of SiC permits us to study anharmonicities in the quantum vibrational motion of carbon and silicon atoms within a binary compound, extending beyond those corresponding to monoatomic materials such as diamond and crystalline silicon. This is particularly observable in the kinetic energy and mean-square displacement of C and Si atoms in 3C-SiC.

The paper is structured as follows. In Sec. II, we present the computational methods used in the calculations, including the tight-binding procedure, path-integral molecular dynamics, and the DFT method. In Sec. III, we outline a harmonic approximation for elastic constants and vibrational density of states, employed to analyze anharmonicities in our results. The internal energy and crystal volume of 3C-SiC, derived from PIMD simulations, are discussed in Secs. IV and V, respectively. Section VI provides results for atomic mean-square displacements. Data on the elastic constants and bulk modulus at finite temperatures are presented in Secs. VII and VIII. Finally, the main outcomes are summarized in Sec. IX.

II. METHOD OF CALCULATION

A. Tight-binding method

We investigate nuclear quantum effects on the structural and elastic properties of 3C-SiC, focusing on the quantum delocalization of atomic nuclei and its impact on various physical properties of the solid. For this purpose, two main components are required. Firstly, a suitable potential is necessary to define interatomic interactions within the material. Such potentials are typically derived from *ab initio* techniques, tight-binding Hamiltonians, or empirical models. This establishes a Born-Oppenheimer surface for nuclear motion. Secondly, a method is needed to account for quantum dynamics in the configuration space of nuclear coordinates, using the chosen interatomic potential. This necessitates finite-temperature simulations grounded in quantum statistical physics, as opposed to the classical statistics often used in atomistic simulations (such as molecular dynamics or Monte Carlo). In this paper, we achieve this through PIMD simulations, described in Sec. II B.

Our simulations are conducted under the adiabatic (Born-Oppenheimer) approximation. The potential energy surface for nuclear dynamics is derived from an effective tight-binding Hamiltonian [44]. While it is possible in principle to employ *ab initio* methods for finite-temperature simulations, such an approach would significantly limit the duration of simulation trajectories or the feasible system size due to computational constraints. The approach we utilize takes into account both the quantum nature of electrons (via the TB Hamiltonian) and atomic nuclei (through the use of path integrals). This allows for the direct inclusion of electron-phonon and phonon-phonon interactions in our PIMD simulations.

We compute interatomic forces and total energies using the nonorthogonal TB Hamiltonian developed by Porezag *et al.* [44], which is grounded in DFT calculations within the local density approximation (LDA). The specific TB parametrization for structures containing both C and Si atoms is detailed in Ref. [45]. In this parametrization, atomic orbitals are obtained as eigenfunctions of appropriately constructed pseudoatoms, with the valence electron charge density situated near the nucleus. The overlap matrices between atomic orbitals and Hamiltonian matrix elements are tabulated as functions of internuclear distance. Additionally, the short-range repulsive portion of the potential is fitted to self-consistent LDA data from relevant reference systems [46]. The nonorthogonality of the atomic basis plays a pivotal role in ensuring the transferability of the TB parametrization to complex systems [44].

This tight-binding model has previously been applied to investigate bulk SiC [47,48], reconstructions of its surfaces [45], as well as isotopic and quantum effects in the cubic phase [42,43]. It has also been employed to study various properties of recently synthesized silicon carbide monolayers [5,49]. A comprehensive review of the capabilities of TB procedures in accurately describing a range of properties in both molecules and condensed matter was provided by Goringe *et al.* [46].

To sample the electronic degrees of freedom in reciprocal space, we consider only the Γ point ($\mathbf{k} = 0$) in this paper. Including larger $\mathbf{k}$ sets in the calculations leads to a slight shift in total energy, but with negligible impact on the energy differences presented below. This shift results in a minor adjustment of the minimum energy E_0, which becomes less pronounced as the cell size increases. Figure 1 illustrates this behavior, displaying the internal energy of unstressed 3C-SiC across various cell sizes. In the figure, solid circles represent the energy attained with the TB model (Γ point) for the minimum-energy configuration ($T = 0$, classical). Additionally, we have plotted outcomes for energy obtained from classical MD simulations (solid squares) and PIMD simulations (open squares) at $T = 300$ K. In both classical and quantum cases, we observe a consistent upward shift of the energy relative to classical results at $T = 0$. Something similar happens for the quantum zero-point energy (open
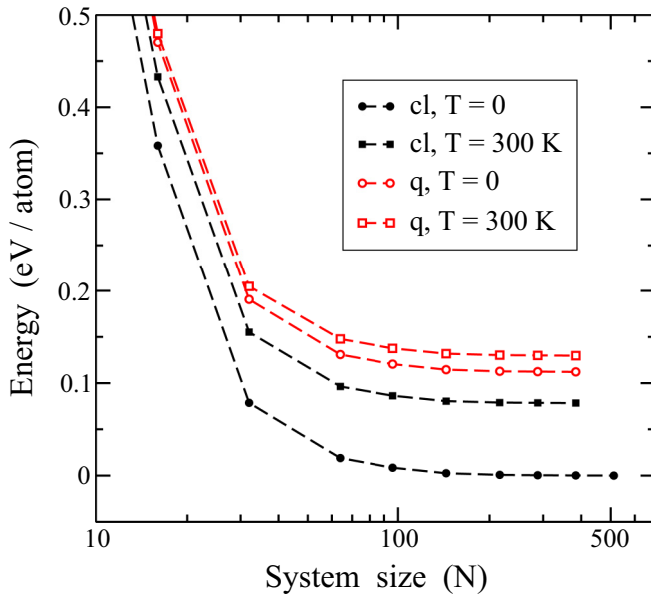
FIG. 1. Energy as a function of system size for $3C$-SiC, calculated with the TB Hamiltonian used in this work. Solid circles: $T = 0$; solid squares: classical MD simulations for $T = 300$ K; open circles: quantum results for $T \to 0$; open squares: PIMD for $T = 300$ K. Labels "cl" and "q" refer to classical and quantum results, respectively. Lines are guides to the eye.

squares) derived from extrapolation of finite-temperature results of PIMD simulations for different cell sizes (see below).

B. Path-integral molecular dynamics

We investigate the equilibrium properties of $3C$-SiC as functions of both temperature and pressure by means of PIMD simulations. This technique is rooted in Feynman's path-integral formulation of statistical mechanics [50], a valuable nonperturbative approach for exploring quantum systems at finite temperatures. In practical implementations of this computational method, each quantum particle (in our context, an atomic nucleus) is represented as a group of N_{Tr} (Trotter number) beads. These beads emulate classical particles, collectively forming a ring polymer [30,31]. This representation establishes a *classical isomorph*, which effectively samples the configuration space, providing accurate values for quantum system properties. For a more comprehensive understanding of this simulation method, additional details can be found elsewhere [30,31,51,52].

We carried out PIMD simulations in the isothermal-isobaric (NPT) ensemble, employing established algorithms outlined in the literature [53–55]. Specifically, we made use of staging coordinates to define the positions of the beads within the classical isomorph. Furthermore, each staging coordinate was coupled to a chain of four Nosé-Hoover thermostats, maintaining a constant temperature throughout the simulations. Additionally, a chain of four thermostats was linked to the barostat, enabling the necessary volume fluctuations to match the targeted pressure [51,56].

The equations of motion were integrated using the reversible reference system propagator algorithm (RESPA),

which allows to use different time steps for the integration of fast and slow degrees of freedom [57]. For the dynamics related to interatomic forces, a time step of $\Delta t = 1$ fs was employed. Meanwhile, the evolution of fast dynamical variables, including harmonic bead interactions and thermostats, was computed with a time step of $\delta t = 0.25$ fs. To calculate the kinetic energy E_{kin}, we used the virial estimator. This choice is particularly advantageous as it exhibits a statistical uncertainty smaller than that of the potential energy, especially at high temperatures [56,58]. Further insights into this type of PIMD simulations can be found in various literature sources [33,54,59].

We conducted simulations using $2 \times 2 \times 2$ and $3 \times 3 \times 3$ supercells of the face-centered cubic unit cell of $3C$-SiC, under periodic boundary conditions. These supercells comprised $N = 64$ and 216 atoms, respectively. We sampled the configuration space for temperatures ranging from 50 to 1500 K and pressures spanning from -30 to 60 GPa. For typical simulation runs, we performed 2×10^5 PIMD steps for system equilibration, followed by 8×10^6 steps to compute average properties. The Trotter number N_{Tr} was set to vary with temperature according to the relation $N_{Tr}T = 6000$ K, approximately ensuring constant precision for PIMD results across different temperatures [33,59]. We have checked that this election of N_{Tr} provides adequate convergence for our quantum model of $3C$-SiC. In particular, we have checked this convergence for $T = 300$ K, considering values of the Trotter number up to $N_{Tr} = 60$, and found results for the variables considered here which coincide within statistical error bars with those found for $N_{Tr} = 20$. Thus, for the energy we obtained differences smaller than 1 meV/atom.

As the system size N increases, the simulations effectively sample vibrational modes with longer wavelengths λ. In practical terms, there exists an effective wavelength cutoff at $\lambda_{max} \approx L$, where $L = na$ (with a being the lattice parameter and n equal to 2 or 3 in our case). This corresponds to a wave-number cutoff of $k_{min} \approx 2\pi/L$, where $k = |\mathbf{k}|$. Given that $N \sim L^3$, we observe that $k_{min} \sim N^{-1/3}$. This wave-number cutoff, coupled with employing a single $\mathbf{k}$ point, could cause a lack of convergence in calculated magnitudes versus system size N. We have verified the agreement of results obtained for $N = 64$ and 216 atoms, specifically for the energy difference $E - E_0$ and the volume V, within statistical error bars.

In order to gauge the magnitude of quantum effects calculated from our PIMD simulations, we also performed classical MD simulations using the same TB Hamiltonian. This corresponds to setting the Trotter number to one, which results in the merging of ring polymers into single beads.

An alternative approach for studying anharmonic effects in condensed matter involves the use of self-consistent phonon or quasiharmonic approximations, where vibrational mode frequencies are assumed to be volume-dependent [22,60–62]. This approach enables the incorporation of temperature effects and reveals anharmonicities at $T = 0$ without the need for extrapolation, as required by path-integral methods. The quasiharmonic approximation has been effectively applied to analyze phenomena such as thermal expansion and isotopic effects in solids [12,21–23], as well as the properties of small clusters [61] and molecules [60].

C. DFT calculations

To assess the accuracy of the employed TB procedure in describing the properties of 3*C*-SiC, we carried out state-of-the-art DFT calculations for this material. For this purpose, we utilized the Quantum-ESPRESSO package for electronic structure calculations [63,64].

In particular, we adopted the Perdew-Burke-Ernzerhof exchange-correlation functional in its solid-state version (PBEsol) [65], along with a plane-wave basis set featuring cutoffs of 45 Ry for the kinetic energy and 400 Ry for the charge density. For both C and Si atoms, projector-augmented-wave (PAW) pseudopotentials were employed [66].

We considered a cubic zinc-blende structure cell of SiC containing 8 atoms subject to periodic boundary conditions. For Brillouin zone integration, we employed a $10 \times 10 \times 10$ Monkhorst-Pack grid [67].

Ab initio electronic-structure calculations have been previously carried out to explore various properties of cubic silicon carbide. These investigations encompass lattice-dynamical, structural, mechanical, electronic, and thermodynamic properties [68–72]. Such calculations have proven highly valuable for investigating the phase diagram of silicon carbide, particularly regarding phase transitions under high pressure [11,14,19,20,73].

III. HARMONIC APPROXIMATION

To asses the relevance of anharmonicity in the results of our PIMD simulations for 3*C*-SiC, we consider a harmonic approximation (HA) for the atomic vibrational modes. While this approximation is generally reliable at low T in solids, anharmonicity typically becomes more pronounced as T increases. This leads to a progressive deviation of the harmonic approach from the more accurate atomistic simulations. Within the HA, frequencies are treated as independent of temperature, thereby excluding considerations of volume changes (thermal expansion).

To establish a reference for the subsequent analysis of thermal and nuclear quantum effects, we assess the elastic stiffness constants, C_{ij}, in the classical low-temperature limit. These elastic constants for 3*C*-SiC at $T = 0$ have been derived from the harmonic dispersion relation of acoustic phonons. This calculation involved diagonalization of the dynamical matrix obtained from the TB Hamiltonian [16].

Sound velocities in a solid can be derived by assessing the slope of acoustic phonon branches close to the Γ point. Specifically, we obtain these velocities by evaluating the derivative $\partial \omega / \partial k$ along high symmetry directions of the Brillouin zone. In the context of cubic crystals, this relation is established as [74,75]

$$C_{11} = \rho \left(\frac{\partial \omega_{\mathrm{LA}}}{\partial k_x} \right)_\Gamma^2, \tag{1}$$

for the longitudinal acoustic (LA) band along the [100] direction, and

$$C_{12} = C_{11} - 2\rho \left(\frac{\partial \omega_{\mathrm{TA}_2}}{\partial k} \right)_\Gamma^2, \tag{2}$$

$$C_{44} = \rho \left(\frac{\partial \omega_{\mathrm{TA}_1}}{\partial k} \right)_\Gamma^2, \tag{3}$$
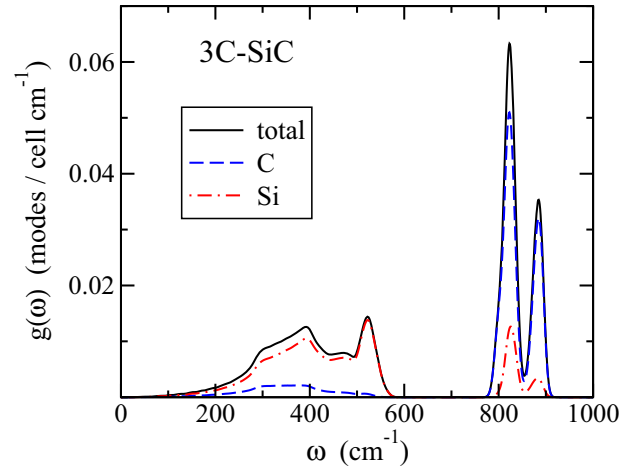

FIG. 2. Vibrational density of states of 3*C* silicon carbide, calculated in the HA for the TB Hamiltonian used in this work. Dashed and dashed-dotted curves depict the VDOS corresponding to carbon, $g_\mathrm{C}(\omega)$, and silicon, $g_\mathrm{Si}(\omega)$, respectively. The solid line represents the total density of states, $g(\omega)$.

for the transverse acoustic bands, TA$_1$ and TA$_2$, along the [110] direction. In these equations, ρ denotes the solid's density. For the HA, our calculations yield the following elastic constants: $C_{11} = 452.9$ GPa, $C_{12} = 141.1$ GPa, and $C_{44} = 246.7$ GPa. We have confirmed that these values align with those obtained for the different phonon bands along other symmetry directions in **k**-space.

The isothermal bulk modulus of cubic crystals can be determined from the elastic constants through the expression [74]:

$$B = \tfrac{1}{3}(C_{11} + 2C_{12}). \tag{4}$$

From this formula, we find a bulk modulus $B_0 = 245.0$ GPa for the minimum-energy configuration (classical minimum).

To directly assess the anharmonicity of atomic vibrations, we have calculated the vibrational density of states (VDOS) for the entire Brillouin zone within the HA. This computation was executed via numerical integration, following the method outlined in Ref. [76]. In Fig. 2, we present the resultant VDOS for 3*C*-SiC, with dashed and dashed-dotted lines denoting the respective contributions from carbon and silicon. The solid line represents the cumulative VDOS encompassing both constituents. We will use the notations $g_\mathrm{C}(\omega)$ and $g_\mathrm{Si}(\omega)$ to call the VDOS contributions from C and Si atoms, while the overall VDOS is expressed as $g(\omega) = g_\mathrm{C}(\omega) + g_\mathrm{Si}(\omega)$.

The quantum-mechanical vibrational energy per atom at temperature T within the HA is given by

$$E_{\mathrm{vib}} = \frac{1}{2N} \sum_{r,\mathbf{k}} \hbar \, \omega_r(\mathbf{k}) \coth \left(\frac{1}{2} \beta \hbar \, \omega_r(\mathbf{k}) \right), \tag{5}$$

where $\beta = 1/k_B T$ (with k_B being Boltzmann's constant). The index r ($r = 1, \ldots, 6$) designates the phonon branches, and the summation over wave vectors **k** traverses the Brillouin zone. Alternatively, based on the continuous approximation of the VDOS $g(\omega)$, the energy E_{vib} can be calculated as

$$E_{\mathrm{vib}} = \frac{1}{4} \int_0^{\omega_{\max}} \hbar \, \omega \coth \left(\frac{1}{2} \beta \hbar \, \omega \right) g(\omega) d\omega, \tag{6}$$
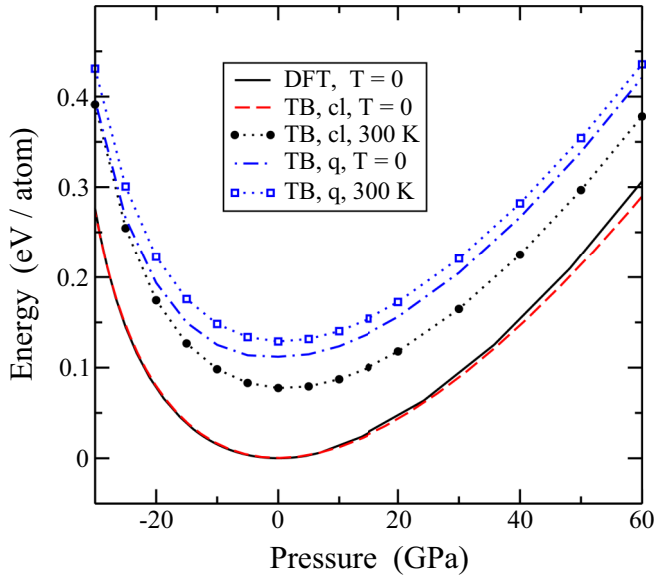
FIG. 3. Energy per atom vs hydrostatic pressure. The solid and dashed lines represent results obtained from DFT and TB calculations, respectively, at $T = 0$. Symbols depict results from classical MD (solid circles) and PIMD simulations (open squares) at $T = 300$ K. The dashed-dotted line represents the quantum limit for $T \to 0$. Labels "cl" and "q" refer to classical and quantum results, respectively. Dotted lines are guides to the eye.

where ω_{max} stands for the maximum frequency in the phonon spectrum. Note that we use the normalization condition

$$\int_0^{\omega_{max}} g(\omega)d\omega = 6, \tag{7}$$

to account for the six degrees of freedom present in a crystallographic unit cell (comprising one C and one Si atom).

IV. ENERGY

In this section, we present and analyze the internal energy of 3C-SiC, extracted from PIMD simulations conducted within the NPT ensemble at various pressures and temperatures. This simulation approach provides distinct evaluations of the potential and kinetic energy of the system [49,51,77]. This enables the exploration of lattice vibration anharmonicities by scrutinizing differences between both energies, which coincide for harmonic systems.

For a specified combination of pressure and temperature, the internal energy can be expressed as $E = E_0 + E_{pot} + E_{kin}$, where E_{pot} and E_{kin} correspond to the potential and kinetic energy, respectively. E_0 denotes the energy of the classical model at zero temperature (minimum-energy configuration). Figure 3 displays the energy difference $E - E_0$ as a function of hydrostatic pressure. The solid and dashed curves portray the energy outcomes derived at $T = 0$ via DFT and TB calculations, respectively. The energy reference is established at the unstressed material state ($P = 0$). The energy curves closely align in the pressure range spanning from a tensile pressure of $P = -30$ GPa to a compressive pressure of approximately 40 GPa. Beyond this interval of compressive stress, a divergence becomes apparent between the TB and DFT energy

curves, the former exhibiting a slower growth rate compared to the latter.

In Fig. 3, symbols are employed to represent the outcomes of simulations performed at $T = 300$ K. Solid circles correspond to classical MD results, while open squares represent PIMD simulations. The classical results exhibit a nearly uniform increase of $3k_BT$ relative to the TB results at $T = 0$. This signifies the contribution of thermal energy per atom at the given temperature. In the case of PIMD simulations, we observe that at a pressure of $P = 0$, there is an enhancement of 51 meV/atom compared to the classical data. This difference in energy grows from 40 to 57 meV/atom within the pressure range spanning from -30 to 60 GPa. The average phonon frequency $\overline{\omega}$ escalates with increasing pressure, leading to an amplification of the energy difference δE between quantum and classical models, especially at relatively low temperatures, including 300 K. The dashed-dotted line in this figure represents the quantum limit of the energy for $T \to 0$, extrapolated from our finite-temperature PIMD simulations in the plotted pressure range. In the low-T limit, the rate of change $\partial(\delta E)/\partial P$ is given by $\frac{3}{2}\hbar \, \partial\overline{\omega}/\partial P > 0$.

In Fig. 4(a), we present the temperature dependence of the internal energy, $E - E_0$, which was obtained from PIMD simulations of cubic SiC at zero pressure, indicated by solid squares. Additionally, we display the internal energy values obtained from classical MD simulations, represented by solid circles. As temperature decreases, the quantum results converge to an energy $E = E_0 + E_{ZP}$, where E_{ZP} is the zero-point energy, which results to be 112 meV/atom. At low temperatures, classical simulations exhibit a dependence described by $E - E_0 \propto T$, in line with predictions derived from the equipartition principle in classical statistical mechanics for harmonic vibrations: $E - E_0 = 3k_BT$. At high temperature, classical MD simulations show slight deviations from this linear dependence due to the anharmonicity of lattice vibrations. Notably, the zero-point energy obtained from PIMD simulations is on the order of the classical thermal energy at 450 K, which corresponds to approximately one third of the material's Debye temperature [29]. As the temperature increases, the results of both PIMD and classical MD simulations gradually converge. However, even at $T = 1000$ K, a difference of 17 meV/atom remains between both sets of data.

In Fig. 4(b), the kinetic energy as a function of temperature is presented. The symbols represent data from our PIMD simulations: circles indicate C atoms, while squares denote Si atoms. The solid and dashed lines on the graph represent the results obtained from the HA for C and Si, respectively. It is noticeable that in both cases, the symbols lie below their corresponding lines. This observation indicates that anharmonicity leads to a reduction in kinetic energy. According to the outcomes of quantum simulations at low temperatures, the kinetic energy for carbon and silicon atoms is 68.3 and 42.0 meV, respectively. This yields a ratio of $E_{kin}^{C}/E_{kin}^{Si} = 1.63$ as the temperature approaches absolute zero. Comparing these low-temperature results to those provided by the HA, it becomes apparent that, due to anharmonicity, there is a reduction of 4% in each case. The dashed-dotted line featured in Fig. 4(b) represents the classical kinetic energy per atom, which remains constant regardless of the atomic mass: $E_{kin} = 3k_BT/2$.
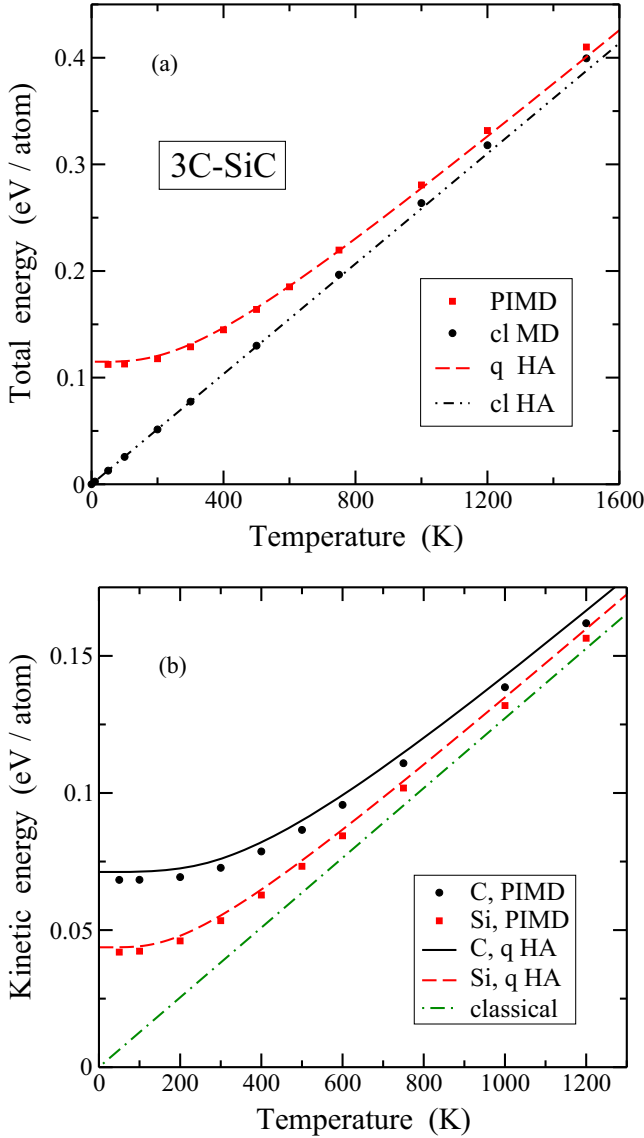
FIG. 4. (a) Energy per atom vs temperature. Symbols display results of classical MD (circles) and PIMD simulations (squares.) The dashed line represents the HA obtained from the VDOS using Eq. (6). The dashed-dotted line depicts the classical thermal energy per atom: $E^{cl} = 3k_BT$. Labels "q" and "cl" refer to quantum and classical results, respectively. (b) Temperature dependence of the kinetic energy of C (solid circles) and Si atoms (solid squares), obtained from PIMD simulations. Solid and dashed lines represent the kinetic energy found from the corresponding VDOS, $g_C(\omega)$ and $g_{Si}(\omega)$, respectively. The dashed-dotted line illustrates the classical kinetic energy $E^{cl}_{kin} = 3k_BT/2$.

An evaluation of lattice-vibration anharmonicity can be achieved by comparing the potential and kinetic energy derived from PIMD simulations. In the context of harmonic vibrations, the expectation is that $E_{pot} = E_{kin}$ (as derived from the virial theorem), so that any deviation of the ratio E_{kin}/E_{pot} from unity is an indication of anharmonicity. In Fig. 5, we present the temperature-dependent behavior of both overall kinetic and potential energy. As before, the symbols on the graph correspond to data obtained from PIMD simulations, while the solid line represents the outcome for the harmonic
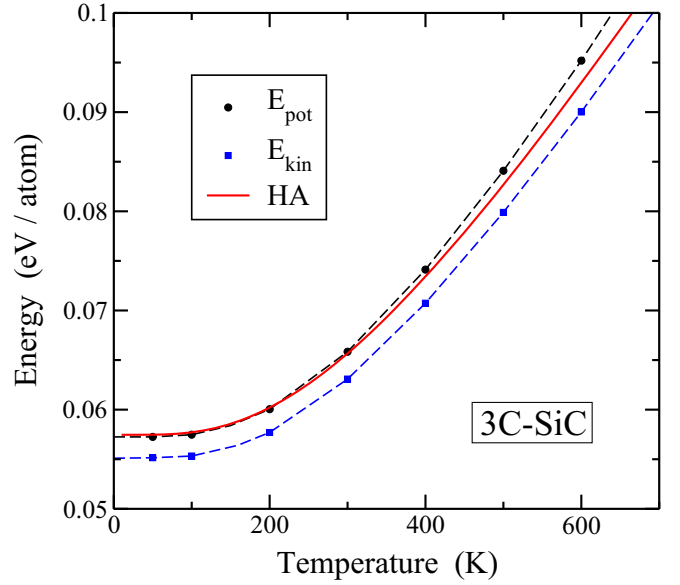

FIG. 5. Mean kinetic (E_{kin}, squares) and potential energy (E_{pot}, circles) per atom vs temperature, as derived from PIMD simulations. The solid line represents the harmonic expectancy obtained from the VDOS as $E_{kin} = E_{pot} = E_{vib}/2$, using Eq. (6). Dashed lines are guides to the eye.

approximation. At low temperatures, a ratio of $E_{pot}/E_{kin} = 1.04$ is obtained. This ratio displays an increase as the temperature rises, reaching a value of 1.08 at 1000 K.

At low temperature, an apparent difference emerges between the potential and kinetic energy. The potential energy tends to closely align with the harmonic expectation, in contrast to the behavior observed for the kinetic energy, as discussed earlier for C and Si atoms. This fact has also been noted in quantum simulations of various other materials and for impurities in crystalline solids [33,78]. The reason behind this can be comprehended by examining energy shifts obtained through time-independent perturbation methods. To illustrate, in the case of a one-dimensional perturbed harmonic oscillator, where the potential energy is given by $V(x) = m\omega^2 x^2/2$ and a perturbation $W(x) = Ax^3 + Bx^4$ is introduced, the first-order variation in the ground-state energy is attributed to a change in kinetic energy, while the potential energy remains unaffected, as in the unperturbed oscillator [78,79]. For a more detailed explanation, we refer to Appendix A.

V. VOLUME

In the case of unstressed 3C-SiC, the volume of the crystal obtained from classical MD simulations displays an almost linear dependence on temperature. The slope $\partial V/\partial T$ of this relationship increases gradually as the temperature rises. At low T, the volume converges toward a value of $V_0 = 10.277$ Å^3/atom, corresponding to the minimum-energy volume (lattice parameter $a_0 = 4.348$ Å). For the purpose of comparison, our DFT calculations yield a minimum-energy volume of $V_0 = 10.346$ Å^3/atom (lattice parameter $a_0 = 4.358$ Å). This value is close to the results obtained from previous *ab initio* studies [14].

For each given temperature T, the volume obtained through quantum PIMD simulations consistently exceeds the corresponding classical value. This trend converges toward a volume of $V_{min} = 10.355$ Å^3/atom as the temperature approaches absolute zero ($a_{min} = 4.359$ Å). Consequently, a zero-point volume expansion of 0.8% in comparison to the classical minimum is observed, translating to a lattice parameter increase of $\delta a = 1.1 \times 10^{-2}$ Å. The simulation results from both the quantum and classical approaches gradually align as the temperature increases. At 300 K, the difference between the two sets of data is approximately half of its value at the low-temperature limit. Remarkably, the outcomes of PIMD simulations employing the TB Hamiltonian closely approximate the experimental data derived from x-ray diffraction of cubic SiC under ambient conditions. Specifically, at 297 K, the experimental lattice parameter was found to be $a = 4.36$ Å [42,80].

The quantum zero-point dilation in a solid is governed by the presence of anharmonicities in its vibrational modes. This has predominantly been explored within a quasiharmonic approximation. In this approach, each individual phonon mode contributes to the $T = 0$ dilation by the product of its zero-point energy and the associated Grüneisen parameter γ_ω [21,22,81]. An alternative approach consists in defining an overall parameter, denoted as $\overline{\gamma}$, derived from the average frequency $\overline{\omega}$ as follows:

$$\overline{\gamma} = -\frac{\partial(\ln \overline{\omega})}{\partial(\ln V)}. \quad (8)$$

This formulation proves valuable in investigating the influence of anharmonicity on the thermodynamic properties of solids [82].

At $T = 0$, the energy E for a specific volume V can be written as the sum of two components: $E = E_{cl} + E_{ZP}$. Here, E_{cl} corresponds to the classical energy as depicted in Fig. 3, and $E_{ZP} = 3\hbar\overline{\omega}/2$ represents the zero-point energy per atom. By employing the equilibrium condition under zero pressure, $\partial E/\partial V = 0$, and referring to Appendix B for more details, we derive the equation:

$$\left(\frac{\partial E_{cl}}{\partial V}\right)_{V_{min}} \approx \frac{\overline{\gamma} E_{ZP}}{V_0}. \quad (9)$$

In this context, V_{min} signifies the volume corresponding to the quantum ground state. Considering the volume dependence of E_{cl}, as given by the TB Hamiltonian, we determine the left-hand side of Eq. (9) to be 1.82 GPa. This computation leads to a value of $\overline{\gamma}$ equal to 1.05, consistent with the Grüneisen parameter values available in the literature for 3C-SiC [10,73]. As a result, the quantum zero-point dilation can be expressed using Eq. (B8) as follows:

$$V_{min} - V_0 = \frac{\overline{\gamma} E_{ZP}}{B_0}. \quad (10)$$

Given a value of $\overline{\gamma}$ equal to 1.05, Eq. (10) yields a volume of $V_{min} = 10.354$ Å^3/atom, which is consistent with the low-temperature volume directly obtained from PIMD simulations.

We will now analyze the influence of hydrostatic pressure on the crystal volume V. In Fig. 6, we display the pressure-induced changes in volume per atom at $T = 0$, as determined
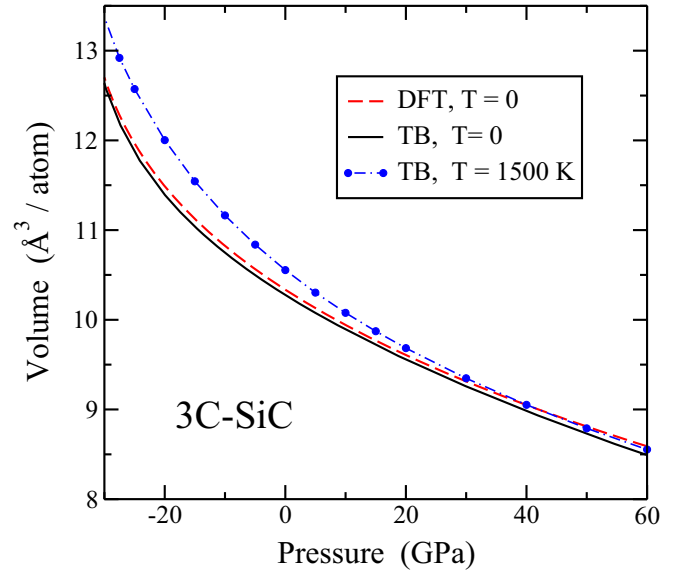

FIG. 6. Volume vs pressure, as obtained from DFT (dashed curve) and tight-binding calculations (solid curve) at $T = 0$. Circles represent results of classical TB MD simulations at 1500 K. Error bars are in the order of the symbol size. The dashed-dotted line is a guide to the eye.

through DFT calculations (depicted by the dashed curve) and TB calculations (represented by the solid curve). These two curves closely align within the pressure range up to approximately 30 GPa, although the DFT result is slightly higher than the TB data. As pressure increases further, the disparity between both datasets gradually becomes more pronounced. The solid circles featured in Fig. 6 denote data points derived from classical MD simulations at $T = 1500$ K. A comparison between these results and the TB calculations at $T = 0$ reveals a notable thermal expansion under tensile pressure. Specifically, this expansion amounts to $\delta V = 0.277$ and 0.604 Å^3/atom for pressures of $P = 0$ and -20 GPa, respectively. In contrast, the volume exhibits a lesser dilation under compression. For instance, at a pressure of $P = 40$ GPa and a temperature of 1500 K, the volume expansion is $\delta V = 0.067$ Å^3/atom.

Results of our PIMD simulations at low temperatures indicate that the volume expansion associated to quantum zero-point motion is also significantly affected by hydrostatic pressure. In fact, for increasing compressive stress, the zero-point volume increase is drastically reduced in comparison to unstressed 3C-SiC. Specifically, for $P = 50$ GPa, the volume change δV as T approaches zero is calculated to be 7×10^{-3} Å^3/atom. This is in contrast to the low-temperature expansion of 8×10^{-2} Å^3/atom observed for cubic SiC at $P = 0$.

The change in volume caused by an applied hydrostatic pressure is linked to the material's bulk modulus B, as discussed in Sec. VIII. According to our classical data at $T = 0$, the rate of volume change, $\partial V/\partial P$, turns out to be -4.19×10^{-2} Å^3/(atom GPa) at $P \to 0$. In contrast, at a temperature of $T = 1000$ K, this derivative amounts to -5.32×10^{-2} Å^3/(atom GPa).

For a cubic crystal subjected to uniaxial pressure (say τ_{xx}), the alteration in volume can be determined using the elastic
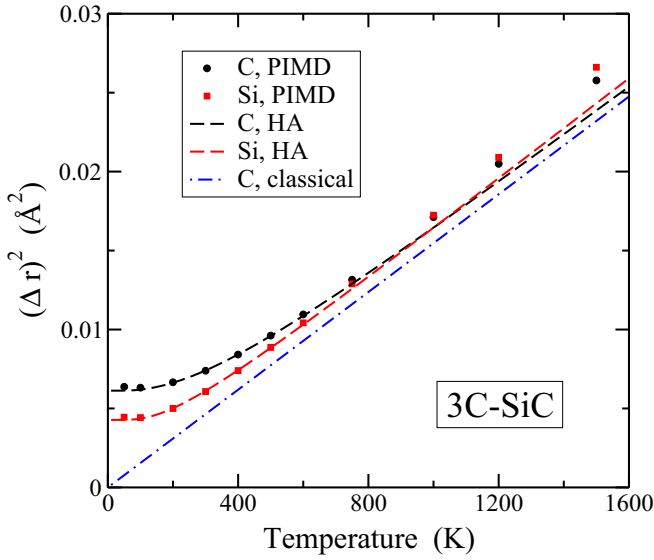
FIG. 7. Atomic mean-square displacement, $(\Delta\mathbf{r})^2$, in $3C$-SiC as a function of temperature. Solid symbols represent results of PIMD simulations for carbon (circles) and silicon (squares). Error bars are in the order of the symbol size. Dashed lines correspond to MSDs for C and Si obtained from the respective VDOS using Eq. (13). The dashed-dotted line represents the carbon MSD obtained in the classical approximation by means of Eq. (14).

compliance constants [74,75,83]:

$$\frac{\delta V}{V} = e_{xx} + e_{yy} + e_{zz} = (S_{11} + 2S_{12})\tau_{xx}. \tag{11}$$

Furthermore, we can derive the stress derivative of volume as follows:

$$\frac{\partial V}{\partial \tau_{xx}} = (S_{11} + 2S_{12})V = \frac{V}{3B}, \tag{12}$$

which provides an alternative formula for computing the bulk modulus through classical MD and PIMD simulations. This approach serves as a method of crossvalidation, thereby enhancing the reliability assessment of our methodology.

VI. ATOMIC MEAN-SQUARE DISPLACEMENTS

In this section, we present an analysis of the atomic mean-square displacement (MSD) in $3C$-SiC, spanning a broad temperature region. The interplay between quantum motion and the anharmonicity of vibrational modes gives rise to discernible effects on the structural and mechanical characteristics of solids, particularly at low temperatures. PIMD simulations offer a means to compute atomic MSDs across varying temperatures. These MSDs encompass both a classical (thermal) part and an intrinsic quantum contribution. The former corresponds to the motion of the center of gravity (centroid) of the quantum paths associated with the atomic nuclei. In contrast, the latter is linked to the average size of the ring polymers that depict the quantum behavior of the nuclei.

In Fig. 7, we display the temperature-dependent behavior of the atomic MSD for C, represented by circles, and Si, represented by squares. These MSD values are derived from PIMD simulations. For $T \to 0$, we determine the squared dis-

placements $(\Delta\mathbf{r})^2$ to be 6.3×10^{-3} Å^2 for C and 4.4×10^{-3} Å^2 for Si atoms, which correspond to zero-point motion. The quotient between these values is close to the inverse square root of the mass ratio, i.e., $(\Delta\mathbf{r})_C^2/(\Delta\mathbf{r})_{Si}^2 \approx (M_{Si}/M_C)^{1/2}$. In the presence of identical effective (harmonic) potentials for both species, these two ratios should strictly coincide. The differing environments of C and Si atoms lead to a difference in these ratios.

The dashed lines depicted in Fig. 7 were generated using the VDOS for C and Si presented in Fig. 2, using the HA. For carbon atoms, this MSD is obtained from the expression:

$$(\Delta\mathbf{r})_C^2 = \int_{\omega_0}^{\omega_{max}} \frac{\hbar}{2\omega M_C} \coth\left(\frac{1}{2}\beta\hbar\omega\right) g_C(\omega)d\omega. \tag{13}$$

A similar expression is utilized for Si, taking into account the atomic mass M_{Si} and the function g_{Si}. At low T, the outcomes of quantum simulations closely align with those yielded by the HA. As the temperature increases, the simulation data progressively surpass the HA predictions. Notably, at approximately $T = 1000$ K, both the simulation results (represented by symbols) and the HA (shown by dashed lines) indicate that $(\Delta\mathbf{r})_{Si}^2$ exceeds $(\Delta\mathbf{r})_C^2$.

The dashed-dotted line in Fig. 7 indicates the MSD of C atoms obtained through a classical HA. In this approximation, one has

$$(\Delta\mathbf{r})_C^2 = \int_{\omega_0}^{\omega_{max}} \frac{k_B T}{\omega^2 M_C} g_C(\omega)d\omega. \tag{14}$$

MSDs obtained from classical calculations are not contingent on atomic mass, but rather they vary in accordance with the effective potential experienced by atomic nuclei. In this specific instance, the interatomic potential experienced by C atoms is relatively "stiffer" compared to that associated with Si atoms. As a result, the classical MSD for silicon becomes larger than that of carbon due to the inherent differences in their effective potentials. This distinction is the reason for the observation that $(\Delta\mathbf{r})_{Si}^2 > (\Delta\mathbf{r})_C^2$ in the quantum calculations at elevated temperatures, as illustrated in Fig. 7.

One way to evaluate the consistency of results from our PIMD simulations, both in position and momentum domains, consists in examining the MSDs $(\Delta\mathbf{r})^2$ and kinetic energy. In accordance with Heisenberg's uncertainty principle, the root-mean-square deviations for the coordinate x and the corresponding momentum p_x of a quantum particle must satisfy the inequality $\Delta x \Delta p_x \geqslant \hbar/2$ (as discussed in, for instance, Ref. [84]). This relationship can also be expressed as

$$(\Delta p_x)^2 \geqslant \frac{\hbar^2}{4(\Delta x)^2}. \tag{15}$$

Similar relations hold for the coordinates y and z.

In our specific case, the average momentum is zero ($\langle\mathbf{p}\rangle = 0$), as usually happens in solids. Thus, for an atomic nucleus with mass M, the kinetic energy can be expressed as

$$E_{kin} = \frac{\langle\mathbf{p}^2\rangle}{2M} = \frac{(\Delta\mathbf{p})^2}{2M}. \tag{16}$$

For cubic crystal structures, where $(\Delta x)^2 = (\Delta y)^2 = (\Delta z)^2$, combining Eqs. (15) and (16) yields

$$E_{\text{kin}} \geqslant \Lambda \equiv \frac{9\hbar^2}{8M(\Delta \mathbf{r})^2}, \qquad (17)$$

where Λ is a function of the atomic MSD. This inequality establishes a lower limit for the kinetic energy, rooted in the particle's spatial extent. In other words, we have $E_{\text{kin}}/\Lambda \geqslant 1$. From the above results for E_{kin} and $(\Delta \mathbf{r})^2$ at low temperature, it is discernible that both C and Si display a ratio of $E_{\text{kin}}/\Lambda = 1.1$. This ratio slightly exceeds the minimum value allowed by the uncertainty relations, and escalates as temperature increases, reflecting a transition toward more classical behavior in atomic motion.

For an isotropic 3D harmonic oscillator characterized by a frequency ω, the MSD for the ground state equates to $3\hbar/(2M\omega)$. Correspondingly, the kinetic energy of the oscillator's ground state is $(E_{\text{kin}})_0 = 3\hbar\omega/4$ [84]. This yields a convergence of E_{kin}/Λ to unity as $T \to 0$, reaching the minimum attainable value. In the context of atomic motion in solids, the dispersion of frequencies can be approximated using an isotropic 3D Debye model (as referenced in Refs. [82,85]), characterized by a vibrational density of states $\rho(\omega) \propto \omega^2$ and a high-frequency cutoff ω_D. In this case, for $T \to 0$ and assuming harmonic vibrations, the ratio E_{kin}/Λ converges to 1.125 (which remains independent of ω_D) [86], near the findings for C and Si atoms from our quantum simulations.

VII. ELASTIC CONSTANTS

In this section, we delve into the influence of nuclear quantum effects on the elastic stiffness constants of 3C-SiC. These effects, akin to other physical observables, become pronounced for various elastic constants, manifesting at temperatures lower than the Debye temperature, Θ_D. The elastic compliance constants, S_{ij}, are evaluated in this study at various temperatures by focusing on specific components of the stress tensor τ_{ij} during isothermal-isobaric simulations. For instance, when $\tau_{xx} \neq 0$ and $\tau_{ij} = 0$ for other components, the relationships $S_{11} = e_{xx}/\tau_{xx}$ and $S_{12} = e_{yy}/\tau_{xx}$ hold true. Here, e_{ij} are the components of the strain tensor determined in the simulations [74,75,82]. Similarly, the evaluation of S_{44} entails the application of a shear stress τ_{xy}, and $S_{44} = e_{xy}/\tau_{xy}$. From these compliance constants, we derive the stiffness constants C_{11} and C_{12} using the cubic crystal relations [74,82]: $C_{11} = (S_{11} + S_{12})/Z$ and $C_{12} = -S_{12}/Z$, where $Z = (S_{11} - S_{12})(S_{11} + 2S_{12})$. Additionally, $C_{44} = 1/S_{44}$. We note that in the context of elasticity, a hydrostatic pressure P corresponds to $\tau_{xx} = \tau_{yy} = \tau_{zz} = -P$.

In Fig. 8, we present the elastic stiffness constants obtained from our simulations of cubic SiC. The graph portrays the temperature dependence of C_{11}, C_{12}, and C_{44} from top to bottom. The results found from classical MD simulations are depicted using solid circles, designated as "cl," while those from PIMD simulations are indicated by squares and shown as "q." The elastic constants derived from classical simulations exhibit a consistent decrease with increasing temperature throughout the range illustrated in Fig. 8. Notably, the extrapolation of these findings to $T = 0$ agrees with the data for C_{ij} derived from the slopes of acoustic phonon bands, as
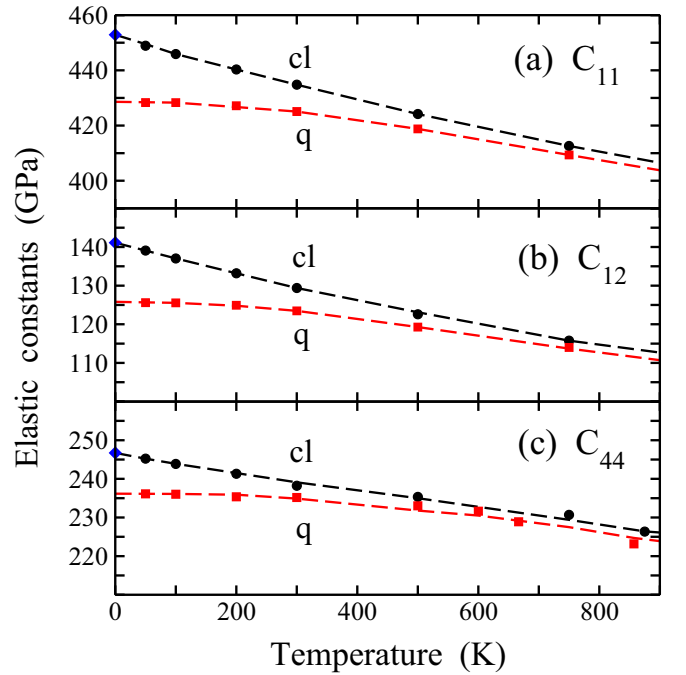

FIG. 8. Temperature dependence of the elastic stiffness constants of cubic silicon carbide: (a) C_{11}, (b) C_{12}, and (c) C_{44}, as derived from classical MD (circles, labeled "cl") and PIMD simulations (squares, labeled "q"). Error bars are in the order of the symbol size. Solid diamonds represent in each case the classical value at $T = 0$, calculated from the phonon dispersion bands. Dashed lines are guides to the eye.

discussed in Sec. III. These $T = 0$ values are represented by solid diamonds on the left vertical axis of Fig. 8.

In Table I, we present a compilation of stiffness constants derived from classical and PIMD simulations at temperatures $T = 300$ and 750 K. Alongside these values, we provide the corresponding classical limits for $T = 0$, computed using the phonon bands methodology (Sec. III). Quantum values for the limit $T \to 0$ are determined by extrapolating finite-temperature PIMD results. A comparison between classical and quantum data reveals that the introduction of zero-point motion yields reductions of approximately 5%, 10%, and 4% for C_{11}, C_{12}, and C_{44}, respectively.

TABLE I. Elastic stiffness constants, bulk modulus, and Poisson's ratio of 3C-SiC, as derived from classical MD and quantum PIMD simulations at $T = 0$, 300 and 750 K. Data for C_{ij} and B are in GPa. Statistical error bars in the last digit are given in parenthesis.

	$T = 0$		$T = 300$ K		$T = 750$ K	
	class.	quantum	class.	quantum	class.	quantum
C_{11}	452.9(5)	428(1)	435(1)	425(2)	413(2)	409(2)
C_{12}	141.1(5)	126(1)	129(1)	123(2)	116(1)	114(2)
C_{44}	246.7(5)	236(1)	238(1)	235(1)	230(2)	228(3)
B	245(1)	227(1)	231(1)	224(1)	215(1)	212(1)
ν	0.238	0.227	0.230	0.224	0.219	0.218

TABLE II. Elastic stiffness constants, bulk modulus B, and Poisson's ratio ν of 3C-SiC derived from results of experimental techniques by different authors at ambient conditions. In each case, the bulk modulus is obtained from the elastic constants by means of Eq. (4). C_{ij} and B are expressed in GPa. Error bars in the last digit, when available, are given in parenthesis.

	Zhuravlev [6]	Lee [7]	Lambrecht [8,9]
C_{11}	391(11)	363	390
C_{12}	122(6)	154	142
C_{44}	253(6)	149	256
B	218(1)	224	225
ν	0.238	0.298	0.267

TABLE III. Elastic stiffness constants, bulk modulus, and Poisson's ratio of 3C-SiC found from several calculations based on density-functional theory with LDA and GGA (PBEsol and PBE), as well as lattice dynamics (LD), an effective potential (EP), and MD simulations. Data for C_{ij} and B are given in GPa. The bulk modulus is calculated in each case from the elastic constants using Eq. (4).

	LD [7]	EP [10]	MD [13]	PBEsol [14]	PBE [11]	LDA [15]
C_{11}	371	371.1	390	390.0	382.9	384
C_{12}	169	223.4	144	137.6	126.9	132
C_{44}	176	279.3	179	246.3	240.9	241
B	225	273	225	224.2	212.2	216
ν	0.313	0.376	0.270	0.261	0.249	0.256

Brito *et al.* [38] conducted an investigation into nuclear quantum effects in diamond utilizing path-integral Monte Carlo simulations with the Tersoff potential. In their analysis, these authors observed a reduction in the elastic constants C_{11} and C_{44} due to quantum nuclear motion, akin to the findings for 3C-SiC. However, their observations regarding C_{12} demonstrated results that were nearly invariant with temperature, coupled with a discernible increase attributed to quantum motion at low T (approximately 5%). This stands in stark contrast to the results depicted in Fig. 8(b). At present, the underlying cause of this disparity remains uncertain. It may stem from the differing characteristics of the cubic materials studied (diatomic versus monoatomic), or to the interatomic potential employed in the simulations.

It is also interesting to compare our results for the elastic constants of cubic SiC with those obtained earlier for graphite using a similar procedure [40]. For graphite, a layered material, a small change was found in C_{11} due to quantum nuclear motion (about 1%) versus 5% obtained here for 3C-SiC, which turns out to be similar to that resulting for diamond [38]. On the contrary, C_{12} undergoes a decrease in cubic SiC (10%), clearly smaller than in graphite (approximately 20%). These differences between cubic and layered materials shed light on anharmonicities associated with lattice vibrations in these types of solids, which manifest themselves in the effect of nuclear motion on magnitudes such as the elastic constants.

It is worth highlighting the correlation between the temperature-dependent behavior of the elastic constants and the atomic MSD. In the case of our classical results for the three stiffness constants, there is a noticeable nearly linear decrease as temperature rises. This behavior is linked to the classical thermal motion of atoms, which in turn leads to a linear growth in the MSD $(\Delta \mathbf{r})^2$ as temperature is raised (as depicted in Fig. 7). Conversely, when examining data obtained from PIMD simulations, a pronounced reduction is observed in the low-temperature elastic constants. This reduction is attributed to the effects of zero-point delocalization, evident in the finite MSD at $T = 0$. As T is elevated, a convergence between classical and quantum data for C_{ij} takes place, much like the convergence observed in the MSD. A similar pattern is also observed in the classical and quantum data for the bulk modulus, as illustrated in Sec. VIII.

In Table II, we give a compilation of C_{ij} values extracted from experimental data as reported by various authors [6–9].

A certain degree of variation is evident in the experimental results obtained under ambient conditions, especially for C_{44}. In particular, the value given in Ref. [7] is notably lower than the other reported values for this stiffness constant. Moving on to Table III, we present a comprehensive overview of elastic constants for cubic silicon carbide calculated by using different computational methodologies. Some calculations were conducted within the framework of DFT, incorporating both LDA [15] and generalized-gradient approximation (GGA) [11,14]. Other results were obtained through lattice-dynamics calculations [7], the utilization of effective interatomic potentials [10], and MD simulations [13].

The Poisson's ratio, ν, is a parameter that characterizes the relationship between transverse and longitudinal strains under an applied stress. For cubic SiC, we calculate it as $\nu = -S_{12}/S_{11}$ [9]. In Table I, we furnish values of Poisson's ratio derived from the elastic constants obtained through our classical and quantum simulations. It is noteworthy that as temperature increases, ν shows a reduction. For $T \to 0$, the influence of zero-point motion causes a decline in ν from 0.238 to 0.227, signifying a reduction of 5%. At $T = 300$ K, the classical and quantum values of ν stand at 0.230 and 0.224, respectively, indicating a decrease of about 3% attributed to quantum motion.

Table II provides the Poisson's ratio values acquired from experimental investigations. Notably, the value derived from the data reported by Zhuravlev *et al.* [6] closely approximates our results, whereas the other two values are relatively higher [7,9]. Table III presents the Poisson's ratio values attained through various theoretical methods. While some dispersion exists in these outcomes, the lowest values correspond to DFT calculations, both within LDA and GGA. These DFT-based results are somewhat higher than our classical result at $T = 0$ ($\nu = 0.238$).

VIII. BULK MODULUS

In this section, we focus on the calculation of the isothermal bulk modulus, $B = -V(\partial P/\partial V)_T$, within our computational approach. As depicted in Fig. 9, we showcase the temperature-dependent behavior of B computed through the elastic constants, using Eq. (4). Solid circles and squares denote the outcomes obtained from classical and PIMD simulations, respectively. The diamond marker positioned at $T = 0$
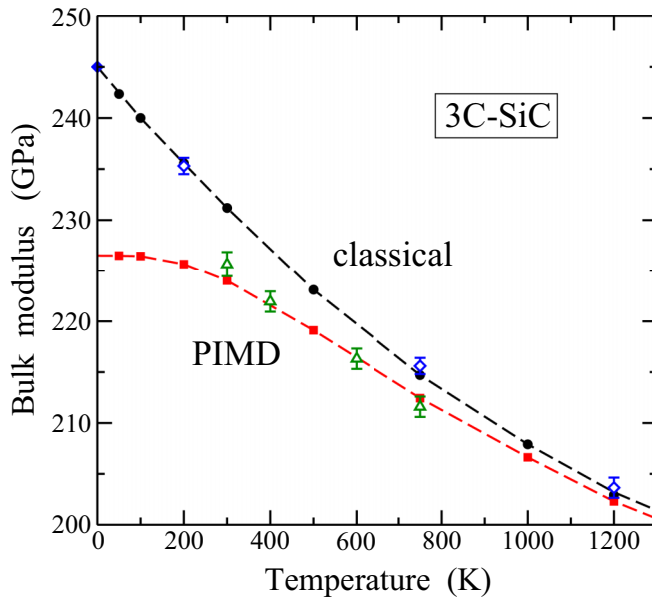
FIG. 9. Temperature dependence of the bulk modulus of 3*C*-SiC, obtained from the elastic constants derived from classical MD (solid circles) and PIMD simulations (solid squares). Error bars of these data are in the order of the symbol size. A solid diamond indicates the classical value for $T = 0$. Open symbols represent data for the bulk modulus found using the fluctuation formula in Eq. (18): diamonds, classical simulations; triangles, PIMD simulations.

signifies the classical value, derived from the phonon bands using the harmonic approximation, as detailed in Sec. III.

The classical results exhibit a nearly linear decrease at low temperatures, accompanied by a substantial slope $\partial B/\partial T$, which becomes less negative as temperature escalates. Notably, at temperatures of 300 and 1200 K, there is a respective reduction in B by 6% and 17% when compared to the low-temperature limit. For decreasing temperature, the extrapolation to $T = 0$ yields values of $B = 245(1)$ GPa and $227(1)$ GPa for classical and quantum simulations, respectively. This signifies a 7% decline in the bulk modulus due to the influence of atomic zero-point motion. The two sets of results converge as temperature increases, with a difference between them of roughly 0.6% at 1000 K. A salient aspect is that the quantum outcomes fulfill the requirement of the third law of Thermodynamics [87,88], namely, that $\partial B/\partial T = 0$ as temperature approaches zero. Conversely, this law is not upheld by the classical data, where $\partial B/\partial T < 0$ remains evident down to $T = 0$.

Table I provides a comprehensive overview of the bulk modulus for 3*C*-SiC. These values are derived by means of Eq. (4), using the stiffness constants obtained through classical and quantum simulations at temperatures of 300 and 750 K, as well as the zero-temperature limit. Additionally, Tables II and III furnish bulk modulus values acquired through experimental and theoretical procedures, respectively. The experimental data for the bulk modulus of cubic SiC obtained by various authors under room temperature conditions closely align with our PIMD simulation result of $B = 224$ GPa at 300 K. Our *ab initio* DFT calculations, carried out without considering nuclear quantum effects at $T = 0$, yield a value

of $B = 224$ GPa, consistent with the findings of Lee and Yao [14], who employed the PBEsol generalized-gradient approximation. Other DFT calculations report values of 212 GPa [11] and 216 GPa [15].

In the context of our classical and quantum atomistic simulations, additional insight into the behavior of the bulk modulus at low temperature can be garnered by means of the fluctuation formula [89]:

$$B = \frac{k_B T V_c}{(\Delta V_c)^2} = \frac{k_B T V}{N (\Delta V)^2}, \tag{18}$$

where $V_c = NV$ signifies the volume of the simulation cell and ΔV represents the volume fluctuations. For a given N, it is observed that $(\Delta V)^2 \sim T$ at low temperatures, regardless of the classical or quantum nature of the simulations. Consequently, the dependence of B on temperature is predominantly governed by the behavior of the function $V(T)$. In a classical model, the volume V increases linearly as temperature rises: $(V - V_0) \sim T$. Conversely, the quantum behavior shows $\partial V/\partial T = 0$ in the low-temperature limit. This distinction is consistent with the observed tendencies at low T: B decreases linearly for rising T in classical simulations, and $\partial B/\partial T \to 0$ for quantum simulations.

Upon analyzing Eq. (18) alongside the actual B values obtained from our simulations, we observe that the change in B attributed to nuclear quantum motion at low temperatures primarily corresponds to an increase in ΔV compared to classical outcomes. Remarkably, our PIMD simulations yield an approximately 7% increase in $(\Delta V)^2$ compared to its classical counterpart, mirroring the shift observed in the bulk modulus B. The variation in the mean volume, V, remains below 1% (refer to Sec. V).

Equation (18) introduces an alternative approach for computing the bulk modulus through simulations. We have verified that this method produces results that align, within error bars, with those obtained from elastic constants employing Eq. (4). Several data points obtained using the fluctuation formula are illustrated in Fig. 9, denoted by open symbols: diamonds represent classical outcomes, while triangles depict quantum data. It is important to note that the error bars associated with this method are comparatively larger than those arising from the determination through elastic constants.

In Fig. 10, we have depicted the relationship between the bulk modulus and hydrostatic pressure. The symbols correspond to results from classical (circles) and PIMD simulations (squares) at $T = 300$ K. The solid line represents the results obtained from DFT calculations at $T = 0$. The TB results at $T = 0$ slightly surpass the classical data at $T = 300$ K, and are omitted for the sake of clarity. As the compressive pressure reaches large values, the DFT result becomes larger that derived from the TB model. This disparity between the two datasets escalates with increasing compressive pressure. Specifically, at $P = 40$ GPa, the difference is approximately 6%.

The DFT results exhibit a pressure derivative of the bulk modulus, $B' = \partial B/\partial P$, which amounts to 3.8 at $P = 0$. In the case of TB data, we observe values of 4.1 and 4.0 for classical and quantum simulations at $T = 300$ K, respectively. Previous DFT calculations have consistently yielded B' values ranging between 3.7 and 3.9 [11,14,15,70]. Moreover,
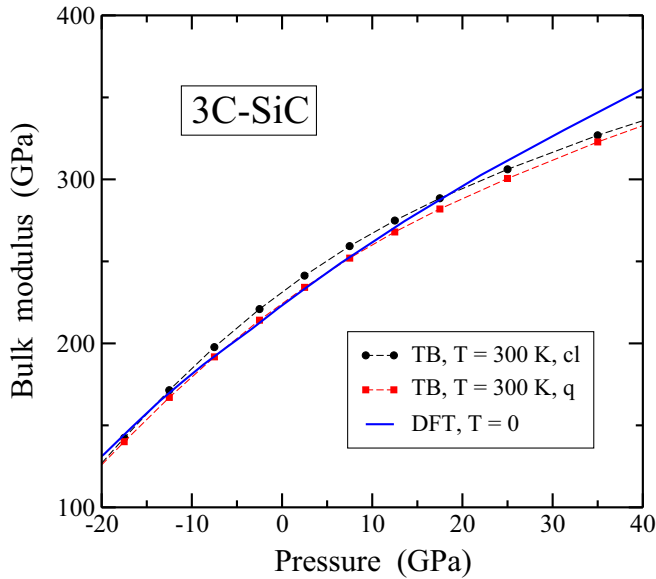
FIG. 10. Bulk modulus of 3C-SiC, as derived from classical MD (circles) and PIMD simulations (squares) at $T = 300$ K for several hydrostatic pressures. Dashed lines are guides to the eye. The solid line represents the results of DFT calculations at $T = 0$. Labels "cl" and "q" refer to classical and quantum data, respectively.

various experimental studies have reported values of the pressure derivative at room temperature spanning from 3.6 to 4 [6,90,91].

It is worth noting that the difference between classical and quantum results for the bulk modulus, δB, diminishes as the pressure increases. In terms of Eq. (18), this is due to a reduction in the difference between quantum and classical MSD $(\Delta V)^2$ for rising hydrostatic pressure, which is associated to an increase in the mean frequency $\overline{\omega}$.

IX. SUMMARY

PIMD simulations provide a robust framework to quantitatively assess nuclear quantum effects on the structural and elastic properties of solids beyond harmonic or quasiharmonic approximations. In the case of silicon carbide, quantum corrections manifest significantly, especially at temperatures below 400 K.

The employment of an effective tight-binding Hamiltonian has enabled precise exploration of the interplay between nuclear quantum motion and anharmonicity, factors that appreciably influence the material's behavior at low temperature. The quality of the TB model in describing the physical properties of 3C-SiC has been established through a direct comparison with DFT calculations at $T = 0$. The pressure-volume equations of state derived from both methods are close to one another in a wide range of pressures, including tensile and compressive stress. For $P \gtrsim 30$ GPa, the bulk modulus derived from TB calculations is smaller than that found using the DFT procedure.

The comparison between PIMD and classical MD simulations emphasizes the importance of nuclear quantum effects in understanding the behavior of SiC. Furthermore, our exploration of anharmonicity using a harmonic approximation

helps to deepen our comprehension of the material's vibrational properties.

The process of quantizing lattice vibrations engenders discernible alterations in the volume and elastic properties of 3C-SiC as compared to a classical model. The quantum zero-point expansion of the volume amounts to about 1% respect the classical prediction. In addition, low-temperature quantum corrections in the elastic stiffness constants C_{11}, C_{12}, and C_{44}, amount to reductions of 5%, 10%, and 4%, respectively. Similar decreases are found for the bulk modulus (7%) and Poisson's ratio (5%). Collectively, our findings underscore the overarching trend: 3C-SiC exhibits a "softer" character than predicted by classical simulations, in particular at low temperature.

We highlight the congruence between our simulation outcomes and the principles of thermodynamics, in particular the third law, which applies for $T \to 0$. Specifically, this alignment implies in our case that the temperature derivatives of the mechanical properties (i.e., elastic constants and bulk modulus) must tend toward null values in the low-temperature limit, contrary to the results of classical simulations.

In contrast to preceding works in this field, our study extends the pressure range to encompass tensile stress ($P < 0$), thereby enabling an examination of SiC within a metastable region of its phase diagram. Additionally, our investigation benefits from a robust foundation for the PIMD simulations, established from direct comparison between TB outcomes and DFT calculations at $T = 0$. Consideration of silicon carbide facilitates an evaluation of the collective impact of anharmonicity and quantum nuclear motion on silicon and carbon atoms within a binary compound, surpassing previous examinations of related monoatomic materials. This is particularly noteworthy in our analysis of MSDs and kinetic energy pertaining to Si and C atoms in 3C-SiC.

In summary, our study emphasizes the advantages of including a quantum description of atomic nuclei into silicon carbide research, significantly impacting our comprehension of its thermal and mechanical attributes. As we broaden our exploration of nuclear quantum effects, it opens the door to an understanding of the involved interralation between phonon quantization and anharmonicity in the physical properties of diverse materials.

APPENDIX A: PERTURBED HARMONIC OSCILLATOR

A qualitative understanding of the low-temperature decrease in kinetic energy with respect to the value expected in a harmonic approximation can be obtained by analyzing changes in kinetic and potential energy by standard time-independent perturbation methods. We consider a one-dimensional harmonic oscillator with potential energy $V(x) = \frac{1}{2}m\omega^2 x^2$, and a perturbation

$$W(x) = Ax^3 + Bx^4. \tag{A1}$$

In static perturbation theory, the perturbed ground state is given to first order by [79,92]

$$E_0^1 = \langle \psi_0^0 | V(x) + W(x) | \psi_0^0 \rangle$$

$$= \frac{1}{2} \hbar \omega + \frac{3}{4} \left(\frac{\hbar}{m\omega} \right)^2 B + o(A^2, B^2). \quad (A2)$$

The superscript in the wave function $|\psi_0^0\rangle$ indicates the unperturbed state. Note that, to first-order, the contribution of the cubic term Ax^3 vanishes.

By calculating separately changes in the kinetic and potential energy in the perturbed oscillator, one finds that the change in ground-state energy, $(\delta E)_0^1 = E_0^1 - E_0^0$, is due to a variation of the kinetic energy, and the potential energy keeps constant for first-order perturbation. This can be seen by calculating the expectation value of the corresponding operators in the first-order-corrected ground state [79,92]:

$$|\psi_0^1\rangle = |\psi_0^0\rangle - \frac{3}{2\sqrt{2}} C_1 A |\psi_1^0\rangle - \frac{3}{2\sqrt{2}} C_2 B |\psi_2^0\rangle$$

$$- \frac{1}{2\sqrt{3}} C_1 A |\psi_3^0\rangle - \frac{\sqrt{3}}{4\sqrt{2}} C_2 B |\psi_4^0\rangle, \quad (A3)$$

where $|\psi_n^0\rangle$ refers to the n'th unperturbed wave function, $C_1 = (\hbar/m^3\omega^5)^{1/2}$ and $C_2 = \hbar/m^2\omega^3$.

Then, for the potential and kinetic energy in the perturbed ground state, $|\psi_0^1\rangle$, we have

$$\langle E_{\text{pot}} \rangle_0^1 = \langle \psi_0^1 | V(x) + W(x) | \psi_0^1 \rangle = \frac{1}{4} \hbar \omega + o(A^2, B^2) \quad (A4)$$

and

$$\langle E_{\text{kin}} \rangle_0^1 = \langle \psi_0^1 | \frac{p^2}{2m} | \psi_0^1 \rangle$$

$$= \frac{1}{4} \hbar \omega + \frac{3}{4} \left(\frac{\hbar}{m\omega} \right)^2 B + o(A^2, B^2). \quad (A5)$$

APPENDIX B: ZERO-TEMPERATURE VOLUME

For a given volume, the energy E at $T = 0$ may be written as $E = E_{\text{cl}} + E_{\text{ZP}}$, where E_{cl} is the classical energy for motionless atoms (given in Fig. 3) and E_{ZP} is the zero-point energy per atom:

$$E_{\text{ZP}} = \frac{1}{2} \int_0^{\omega_{\max}} \frac{1}{2} \hbar \omega \, g(\omega) \, d\omega = \frac{3}{2} \hbar \, \overline{\omega}, \quad (B1)$$

where $\overline{\omega}$ is the mean frequency:

$$\overline{\omega} = \frac{1}{6} \int_0^{\omega_{\max}} \omega \, g(\omega) \, d\omega, \quad (B2)$$

and the factor $1/6$ in front of the integral comes from the normalization condition in Eq. (7). The Grüneisen parameter $\overline{\gamma}$ is defined as

$$\overline{\gamma} = -\frac{\partial (\ln \overline{\omega})}{\partial (\ln V)} = -\frac{V}{\overline{\omega}} \frac{\partial \overline{\omega}}{\partial V}, \quad (B3)$$

and using Eqs. (B1) and (B3), we have

$$\frac{\partial E_{\text{ZP}}}{\partial V} = \frac{3\hbar}{2} \frac{\partial \overline{\omega}}{\partial V} = -\frac{\overline{\gamma} E_{\text{ZP}}}{V}. \quad (B4)$$

For equilibrium at $P = 0$, the volume derivative of the energy E has to vanish, i.e.,

$$\left(\frac{\partial E_{\text{cl}}}{\partial V} \right)_{V_{\min}} = -\left(\frac{\partial E_{\text{ZP}}}{\partial V} \right)_{V_{\min}} \approx \frac{\overline{\gamma} E_{\text{ZP}}}{V_0}, \quad (B5)$$

which gives the volume $V_{\min}$ corresponding to the quantum ground state.

We finally evaluate the zero-point volume expansion due to quantum motion, i.e., the difference $V_{\min} - V_0$. Taking into account that

$$E_{\text{cl}} = E_0 + \frac{1}{2} \frac{B_0}{V_0} (V - V_0)^2 + \cdots, \quad (B6)$$

a good estimation of the volume increase is given by the expression

$$\left(\frac{\partial E_{\text{cl}}}{\partial V} \right)_{V_{\min}} = \frac{B_0}{V_0} (V_{\min} - V_0). \quad (B7)$$

As a result of Eqs. (B5) and (B7), we have

$$V_{\min} = V_0 + \frac{\overline{\gamma} E_{\text{ZP}}}{B_0}. \quad (B8)$$

[1] P. Melinon, B. Masenelli, F. Tournus, and A. Perez, Playing with carbon and silicon at the nanoscale, Nat. Mater. **6**, 479 (2007).

[2] H. C. Hsueh, G. Y. Guo, and S. G. Louie, Excitonic effects in the optical properties of a SiC sheet and nanotubes, Phys. Rev. B **84**, 085404 (2011).

[3] Z. Shi, Z. Zhang, A. Kutana, and B. I. Yakobson, Predicting two-dimensional silicon carbide mono layers, ACS Nano **9**, 9802 (2015).

[4] S. Chabi, Z. Guler, A. J. Brearley, A. D. Benavidez, and T. S. Luk, The creation of true two-dimensional silicon carbide, Nanomaterials **11**, 1799 (2021).

[5] C. M. Polley, H. Fedderwitz, T. Balasubramanian, A. A. Zakharov, R. Yakimova, O. Bäcke, J. Ekman, S. P. Dash, S. Kubatkin, and S. Lara-Avila, Bottom-up growth of monolayer honeycomb SiC, Phys. Rev. Lett. **130**, 076203 (2023).

[6] K. K. Zhuravlev, A. F. Goncharov, S. N. Tkachev, P. Dera, and V. B. Prakapenka, Vibrational, elastic, and structural properties of cubic silicon carbide under pressure up to 75 GPa: Implication for a primary pressure scale, J. Appl. Phys. **113**, 113503 (2013).

[7] D. H. Lee and J. D. Joannopoulos, Simple scheme for deriving atomic force-constants: Application to SiC, Phys. Rev. Lett. **48**, 1846 (1982).

[8] D. W. Feldman, J. H. Parker, W. J. Choyke, and L. Patrick, Phonon dispersion curves by Raman scattering in SiC polytypes 3C, 4H, 6H, 15R, and 21R, Phys. Rev. **173**, 787 (1968).

[9] W. R. L. Lambrecht, B. Segall, M. Methfessel, and M. Vanschilfgaarde, Calculated elastic-constants and deformation potentials of cubic SiC, Phys. Rev. B **44**, 3685 (1991).

[10] D. Varshney, S. Shriya, M. Varshney, N. Singh, and R. Khenata, Elastic and thermodynamical properties of cubic (3C) silicon carbide under high pressure and high temperature, J. Theor. Appl. Phys. **9**, 221 (2015).

[11] Z. Ran, C. Zou, Z. Wei, H. Wang, R. Zhang, and N. Fang, Phase transitions and elastic anisotropies of SiC polymorphs under high pressure, Ceram. Inter. **47**, 6187 (2021).

[12] P. Pertierra, M. A. Salvado, R. Franco, and J. Manuel Recio, Pressure and temperature stability boundaries of cubic SiC polymorphs: A first-principles investigation, Phys. Chem. Chem. Phys. **24**, 16228 (2022).

[13] F. Shimojo, I. Ebbsjo, R. K. Kalia, A. Nakano, J. P. Rino, and P. Vashishta, Molecular dynamics simulation of structural transformation in silicon carbide under pressure, Phys. Rev. Lett. **84**, 3338 (2000).

[14] W. H. Lee and X. H. Yao, First principle investigation of phase transition and thermodynamic properties of SiC, Comput. Mater. Sci. **106**, 76 (2015).

[15] C. Z. Wang, R. C. Yu, and H. Krakauer, Pressure dependence of born effective charges, dielectric constant, and lattice dynamics in SiC, Phys. Rev. B **53**, 5430 (1996).

[16] C. P. Herrero, R. Ramírez, and G. Herrero-Saboya, Cubic silicon carbide under tensile pressure: Spinodal instability, Chem. Phys. **573**, 112005 (2023).

[17] C. Nisr, Y. Meng, A. A. MacDowell, J. Yan, V. Prakapenka, and S. H. Shim, Thermal expansion of SiC at high pressure-temperature and implications for thermal convection in the deep interiors of carbide exoplanets, J. Geophys. Res. Planets **122**, 124 (2017).

[18] D. Kim, R. F. Smith, I. K. Ocampo, F. Coppari, M. C. Marshall, M. K. Ginnane, J. K. Wicks, S. J. Tracy, M. Millot, A. Lazicki, J. R. Rygg, J. H. Eggert, and T. S. Duffy, Structure and density of silicon carbide to 1.5 TPa and implications for extrasolar planets, Nat. Commun. **13**, 2260 (2022).

[19] Y. Kidokoro, K. Umemoto, K. Hirose, and Y. Ohishi, Phase transition in SiC from zinc-blende to rock-salt structure and implications for carbon-rich extrasolar planets, Am. Mineral. **102**, 2230 (2017).

[20] C. Shahi, J. Sun, and J. P. Perdew, Accurate critical pressures for structural phase transitions of group IV, III-V, and II-VI compounds from the scan density functional, Phys. Rev. B **97**, 094111 (2018).

[21] N. Mounet and N. Marzari, First-principles determination of the structural, vibrational and thermodynamic properties of diamond, graphite, and derivatives, Phys. Rev. B **71**, 205214 (2005).

[22] A. Debernardi and M. Cardona, Isotopic effects on the lattice constant in compound semiconductors by perturbation theory: An *ab initio* calculation, Phys. Rev. B **54**, 11305 (1996).

[23] M. Destefanis, C. Ravoux, A. Cossard, and A. Erba, Thermo-elasticity of materials from quasi-harmonic calculations, Minerals **9**, 16 (2019).

[24] M. Kaczmarski, O. N. Bedoya-Martinez, and E. R. Hernandez, Phase diagram of silicon from atomistic simulations, Phys. Rev. Lett. **94**, 095701 (2005).

[25] V. I. Ivashchenko, P. E. A. Turchi, and V. I. Shevchenko, Simulations of the mechanical properties of crystalline, nanocrystalline, and amorphous SiC and silicon, Phys. Rev. B **75**, 085209 (2007).

[26] A. Kubo, S. Nagao, and Y. Umeno, Molecular dynamics study of deformation and fracture in SiC with angular dependent potential model, Comput. Mater. Sci. **139**, 89 (2017).

[27] W. Chen and L.-S. Li, The study of the optical phonon frequency of 3C-SiC by molecular dynamics simulations with deep neural network potential, J. Appl. Phys. **129**, 244104 (2021).

[28] K. W. Kayang and A. N. Volkov, Mechanical properties, phase transitions, and fragmentation mechanisms of 6h, 3C, and amorphous SiC nanoparticles under compression, Appl. Phys. A **127**, 921 (2021).

[29] A. Zywietz, K. Karch, and F. Bechstedt, Influence of polytypism on thermal properties of silicon carbide, Phys. Rev. B **54**, 1791 (1996).

[30] M. J. Gillan, The quantum simulation of hydrogen in metals, Philos. Mag. A **58**, 257 (1988).

[31] D. M. Ceperley, Path-integrals in the theory of condensed helium, Rev. Mod. Phys. **67**, 279 (1995).

[32] B. G. A. Brito, L. Candido, G. Q. Hai, and F. M. Peeters, Quantum effects in a free-standing graphene lattice: Path-integral against classical Monte Carlo simulations, Phys. Rev. B **92**, 195416 (2015).

[33] C. P. Herrero and R. Ramírez, Quantum effects in graphene monolayers: Path-integral simulations, J. Chem. Phys. **145**, 224701 (2016).

[34] J. C. Noya, C. P. Herrero, and R. Ramírez, Thermodynamic properties of crystalline silicon derived by quantum path-integral Monte Carlo simulations, Phys. Rev. B **53**, 9869 (1996).

[35] F. Calvo and Y. Magnin, Nuclear quantum effects on the thermal expansion coefficient of hexagonal boron nitride monolayer, Eur. Phys. J. B **89**, 56 (2016).

[36] B. G. A. Brito, L. C. DaSilva, G. Q. Hai, and L. Candido, Anharmonic quantum effects in cubic boron nitride crystal by path integral Monte Carlo simulations, Phys. Status Solidi B **256**, 1900164 (2019).

[37] R. Ramírez, C. P. Herrero, and E. R. Hernández, A path-integral molecular dynamics simulation of diamond, Phys. Rev. B **73**, 245202 (2006).

[38] B. G. A. Brito, G. Q. Hai, and L. Candido, Quantum effects on elastic constants of diamond by path-integral Monte Carlo simulations, Comput. Mater. Sci. **173**, 109387 (2020).

[39] C. P. Herrero and R. Ramírez, Nuclear quantum effects in graphene bilayers, J. Chem. Phys. **150**, 204707 (2019).

[40] C. P. Herrero and R. Ramírez, Quantum effects in the structural and elastic properties of graphite: Path-integral simulations, Phys. Rev. B **104**, 054113 (2021).

[41] B. G. A. Brito, L. Candido, J. N. Teixeira Rabelo, and G. Q. Hai, Path-integral Monte Carlo simulations on the thermodynamic properties of single-layer hexagonal boron nitride, Comput. Condens. Matter. **31**, e00660 (2022).

[42] R. Ramírez, C. P. Herrero, E. R. Hernández, and M. Cardona, Path-integral molecular dynamics simulation of 3C-SiC, Phys. Rev. B **77**, 045210 (2008).

[43] C. P. Herrero, R. Ramírez, and M. Cardona, Isotope effects on the lattice parameter of cubic SiC, Phys. Rev. B **79**, 012301 (2009).

[44] D. Porezag, Th. Frauenheim, Th. Köhler, G. Seifert, and R. Kaschner, Construction of tight-binding-like potentials on the

basis of DFT theory: application to carbon, Phys. Rev. B **51**, 12947 (1995).

[45] R. Gutierrez, T. Frauenheim, T. Köhler, and G. Seifert, Stability of silicon carbide structures: From clusters to solid surfaces, J. Mater. Chem. **6**, 1657 (1996).

[46] C. M. Goringe, D. R. Bowler, and E. Hernández, Tight-binding modelling of materials, Rep. Prog. Phys. **60**, 1447 (1997).

[47] J. L. Mercer, Tight-binding models for compounds: Application to SiC, Phys. Rev. B **54**, 4650 (1996).

[48] N. Bernstein, H. J. Gotsis, D. A. Papaconstantopoulos, and M. J. Mehl, Tight-binding calculations of the band structure and total energies of the various polytypes of silicon carbide, Phys. Rev. B **71**, 075203 (2005).

[49] C. P. Herrero and R. Ramírez, Quantum effects in two-dimensional silicon carbide, J. Phys. Chem. Solids **171**, 110980 (2022).

[50] R. P. Feynman, *Statistical Mechanics* (Addison-Wesley, New York, 1972).

[51] C. P. Herrero and R. Ramírez, Path-integral simulation of solids, J. Phys.: Condens. Matter **26**, 233201 (2014).

[52] C. Cazorla and J. Boronat, Simulation and understanding of atomic and molecular quantum crystals, Rev. Mod. Phys. **89**, 035003 (2017).

[53] M. E. Tuckerman, B. J. Berne, and G. J. Martyna, Reversible multiple time scale molecular dynamics, J. Chem. Phys. **97**, 1990 (1992).

[54] M. E. Tuckerman and A. Hughes, Path integral molecular dynamics: a computational approach to quantum statistical mechanics, in *Classical and Quantum Dynamics in Condensed Phase Simulations*, edited by B. J. Berne, G. Ciccotti, and D. F. Coker (Word Scientific, Singapore, 1998), p. 311.

[55] G. J. Martyna, A. Hughes, and M. E. Tuckerman, Molecular dynamics algorithms for path integrals at constant pressure, J. Chem. Phys. **110**, 3275 (1999).

[56] M. E. Tuckerman, *Statistical Mechanics: Theory and Molecular Simulation* (Oxford University Press, Oxford, 2010).

[57] G. J. Martyna, M. E. Tuckerman, D. J. Tobias, and M. L. Klein, Explicit reversible integrators for extended systems dynamics, Mol. Phys. **87**, 1117 (1996).

[58] M. F. Herman, E. J. Bruskin, and B. J. Berne, On path-integral Monte Carlo simulations, J. Chem. Phys. **76**, 5150 (1982).

[59] C. P. Herrero, R. Ramírez, and E. R. Hernández, Hydrogen and muonium in diamond: A path-integral molecular dynamics simulation, Phys. Rev. B **73**, 245211 (2006).

[60] F. Calvo, P. Parneix, and N. T. Van-Oanh, Finite-temperature infrared spectroscopy of polycyclic aromatic hydrocarbon molecules. II. Principal mode analysis and self-consistent phonons, J. Chem. Phys. **133**, 074303 (2010).

[61] S. Shimamura, S. N. Khanna, and P. Jena, Self-consistent phonon approach to thermal vibrations in model small clusters, Phys. Rev. B **40**, 2459 (1989).

[62] T. R. Koehler, Theory of self-consistent harmonic approximation with application to solid neon, Phys. Rev. Lett. **17**, 89 (1966).

[63] P. Giannozzi, S. Baroni, N. Bonini, M. Calandra, R. Car, C. Cavazzoni, D. Ceresoli, G. L. Chiarotti, M. Cococcioni, I. Dabo, A. Dal Corso, S. de Gironcoli, S. Fabris, G. Fratesi, R. Gebauer, U. Gerstmann, C. Gougoussis, A. Kokalj, M. Lazzeri, L. Martin-Samos *et al.*, Quantum espresso: a modular and open-source software project for quantum simulations of materials, J. Phys.: Condens. Matter **21**, 395502 (2009).

[64] P. Giannozzi, O. Andreussi, T. Brumme, O. Bunau, M. B. Nardelli, M. Calandra, R. Car, C. Cavazzoni, D. Ceresoli, M. Cococcioni, N. Colonna, I. Carnimeo, A. Dal Corso, S. de Gironcoli, P. Delugas, R. A. DiStasio Jr, A. Ferretti, A. Floris, G. Fratesi, G. Fugallo *et al.*, Advanced capabilities for materials modelling with quantum espresso, J. Phys.: Condens. Matter **29**, 465901 (2017).

[65] J. P. Perdew, A. Ruzsinszky, G. I. Csonka, O. A. Vydrov, G. E. Scuseria, L. A. Constantin, X. Zhou, and K. Burke, Restoring the density-gradient expansion for exchange in solids and surfaces, Phys. Rev. Lett. **100**, 136406 (2008).

[66] Pseudopotentials for C and Si atoms were taken from the *Quantum Espresso PseudoPotential Download Page*: http://www.quantum-espresso.org/legacy_tables, files: C.pbesol-n-kjpaw_psl.1.0.0.UPF, Si.pbesol-n-kjpaw_psl.1.0.0.UPF.

[67] H. J. Monkhorst and J. D. Pack, Special points for Brillouin-zone integrations, Phys. Rev. B **13**, 5188 (1976).

[68] N. Churcher, K. Kunc, and V. Heine, Calculated ground-state properties of silicon carbide, J. Phys. C: Solid State Phys. **19**, 4413 (1986).

[69] C. H. Park, B. H. Cheong, K. H. Lee, and K. J. Chang, Structural and electronic properties of cubic, 2H, 4H, and 6H SiC, Phys. Rev. B **49**, 4485 (1994).

[70] K. Karch, P. Pavone, W. Windl, O. Schutt, and D. Strauch, *Ab-initio* calculation of structural and lattice-dynamical properties of silicon-carbide, Phys. Rev. B **50**, 17054 (1994).

[71] P. Käckell, B. Wenzien, and F. Bechstedt, Electronic-properties of cubic and hexagonal SiC polytypes from *ab initio* calculations, Phys. Rev. B **50**, 10761 (1994).

[72] E. Cannuccia and A. Gali, Thermal evolution of silicon carbide electronic bands, Phys. Rev. Mater. **4**, 014601 (2020).

[73] K. J. Chang and M. L. Cohen, *Ab-initio* pseudopotential study of structural and high-pressure properties of SiC, Phys. Rev. B **35**, 8196 (1987).

[74] C. Kittel, *Introduction to Solid State Physics*, 8th ed. (Wiley, New York, 2005).

[75] P. Y. Yu and M. Cardona, *Fundamentals of Semiconductors* (Springer, Berlin, 1996).

[76] R. Ramírez and M. C. Böhm, Simple geometric generation of special points in Brillouin-zone integrations. Two-dimensional Bravais lattices, Int. J. Quantum Chem. **30**, 391 (1986).

[77] R. Ramírez and C. P. Herrero, Kinetic energy of protons in ice ih and water: A path integral study, Phys. Rev. B **84**, 064130 (2011).

[78] C. P. Herrero and R. Ramírez, Path-integral Monte Carlo simulation of hydrogen in crystalline silicon, Phys. Rev. B **51**, 16761 (1995).

[79] L. D. Landau and E. M. Lifshitz, *Quantum Mechanics*, 2nd ed. (Pergamon Press, Oxford, 1965).

[80] G. A. Slack and S. F. Bartran, Thermal-expansion of some diamond-like crystals, J. Appl. Phys. **46**, 89 (1975).

[81] C. P. Herrero and R. Ramírez, Isotopic effects in structural properties of graphene, Eur. Phys. J. B **93**, 146 (2020).

[82] N. W. Ashcroft and N. D. Mermin, *Solid State Physics* (Saunders College, Philadelphia, 1976).

[83] M. Rabiei, A. Palevicius, A. Dashti, S. Nasiri, A. Monshi, A. Vilkauskas, and G. Janusas, Measurement modulus of elasticity related to the atomic density of planes in unit cell of crystal lattices, Materials **13**, 4380 (2020).

[84] C. Cohen-Tannoudji, B. Liu, and F. Lalöe, *Quantum Mechanics*, 2nd ed. (Wiley, New York, 2020), Vol. 1.

[85] C. Kittel, *Introduction to Solid State Physics*, 7th ed. (Wiley, New York, 1996).

[86] C. P. Herrero and R. Ramírez, Nuclear quantum effects in graphane, Chem. Phys. **533**, 110737 (2020).

[87] H. B. Callen, *Thermodynamics and an Introduction to Thermostatistics* (John Wiley, New York, 1985).

[88] R. S. Berny, S. A. Rice, and J. Ross, *Physical Chemistry* (Oxford University Press, New York, 2000).

[89] L. D. Landau and E. M. Lifshitz, *Statistical Physics*, 3rd ed. (Pergamon Press, Oxford, 1980).

[90] K. Strössner, M. Cardona, and W. J. Choyke, High-pressure X-ray-investigations on 3C-SiC, Solid State Commun. **63**, 113 (1987).

[91] M. Yoshida, A. Onodera, M. Ueno, K. Takemura, and O. Shimomura, Pressure-induced phase-transition in SiC, Phys. Rev. B **48**, 10587 (1993).

[92] C. Cohen-Tannoudji, B. Liu, and F. Lalöe, *Quantum Mechanics*, 2nd ed. (Wiley, New York, 2020), Vol. 2.